Biomedical Physics & Engineering Express

Endorsed by IPEM Institute of Physics and Engineering in Medicine

ACCEPTED MANUSCRIPT • OPEN ACCESS

Thermal damage to the skin from 8.2 and 95 GHz microwave exposures in swine

To cite this article before publication: James E Parker *et al* 2024 *Biomed. Phys. Eng. Express* in press https://doi.org/10.1088/2057-1976/ad488e

Manuscript version: Accepted Manuscript

Accepted Manuscript is "the version of the article accepted for publication including all changes made as a result of the peer review process, and which may also include the addition to the article by IOP Publishing of a header, an article ID, a cover sheet and/or an 'Accepted Manuscript' watermark, but excluding any other editing, typesetting or other changes made by IOP Publishing and/or its licensors"

This Accepted Manuscript is **© 2024 The Author(s). Published by IOP Publishing Ltd**.

As the Version of Record of this article is going to be / has been published on a gold open access basis under a CC BY 4.0 licence, this Accepted Manuscript is available for reuse under a CC BY 4.0 licence immediately.

Everyone is permitted to use all or part of the original content in this article, provided that they adhere to all the terms of the licence https://creativecommons.org/licences/by/4.0

Although reasonable endeavours have been taken to obtain all necessary permissions from third parties to include their copyrighted content within this article, their full citation and copyright line may not be present in this Accepted Manuscript version. Before using any content from this article, please refer to the Version of Record on IOPscience once published for full citation and copyright details, as permissions may be required. All third party content is fully copyright protected and is not published on a gold open access basis under a CC BY licence, unless that is specifically stated in the figure caption in the Version of Record.

View the article online for updates and enhancements.

This content was downloaded from IP address 173.73.27.192 on 10/05/2024 at 14:28

Thermal damage to the skin from 8.2 and 95 GHz microwave exposures in swine

J E Parker[1], J W Butterworth[1], R A Rodriguez[1], C J Kowalczewski[2], R J Christy[2], W B Voorhees[3], J A Payne[3] and J N Whitmore[3]

[1] General Dynamics Information Technology, 4141 Petroleum Road, JBSA Fort Sam Houston, Texas, USA

[2] US Army Institute for Surgical Research, 3698 Chambers Pass, JBSA Fort Sam Houston, Texas, USA

[3] Radio Frequency Bioeffects Branch, 4141 Petroleum Road, JBSA Fort Sam Houston, Texas, USA

E-mail: james.parker.28.ctr@us.af.mil

Abstract. A study of burn thresholds from superficially penetrating radio-frequency (RF) energy at 8.2 and 95 GHz for swine skin was conducted. The study determined the thresholds for superficial, partial-thickness, and full-thickness burn severities after 5 seconds of exposure at power densities of 4–30 W/cm^2 and 2–15 W/cm^2 at 8.2 and 95 GHz, respectively. There were significant differences in the burn thresholds at the different severities between the two frequencies due to the large difference in energy penetration depths. Biopsies were collected from each burn site at 1, 24, 72, and 168 hr post exposure. Each sample was assessed by a burn pathologist against 20 histological factors to characterize the damage resulting from these RF overexposures. A one-dimensional, layered digital phantom that utilized realistic values for dielectric and thermal properties was used to explain some observed thresholds. The results of the heating and cooling response of the animal model, and histology scores of each exposure are provided to enhance future efforts at simulation of RF overexposures and to establish damage thresholds.

Submitted to: *Biomedical Physics and Engineering Express*

Accepted Manuscript

1. Introduction

The radio-frequency (RF) radiation safety guidelines set by the IEEE C95.1 (2019) and the International Commission on Non-Ionizing Radiation Protection (ICNIRP 2020) are generally based upon determining exposure levels that could cause an excessive temperature rise anywhere in the body. Safety factors of 10–50× below these threshold levels are then applied to account for the uncertainty in measured dose and variability in biophysical parameters (e.g., dielectric properties). The reasons for this choice of a threshold are described in the standards, but basically, the threshold provides a conservative estimate of the non-hazardous use of RF energy. However, the safety margins are not constant over the entire RF frequency band, and data that shows the damage thresholds associated with RF overexposure in the band of 6–300 GHz may be helpful to supplement the RF standards to enable a risk-based approach for managing exposures to personnel. Foster *et al* (2020) has suggested that fluence thresholds for pulsed GHz exposures may be overly conservative. In the specific case of millimeter wave (MMW) exposures at 95 GHz, over a thousand people have been shown to be safely self-limiting and non-injurious at levels that are more than 70× the IEEE recommended safety level in restricted environments (Miller *et al* 2021, IEEE 2019). But data on damage threshold levels is sparse, and using rate-process models for estimating damage requires verification. To address these gaps in the upper GHz band, others have asked for empirical studies to help inform model development (Mattsson *et al* 2021, Hirata *et al* 2021, Foster, Ziskin & Balzano 2021, Foster & Vijayalaxmi 2021). This study attempts to help address both of those concerns by providing thermal responses and histological assessments of 352 trials on swine skin. Incorporating the 8.2 and 95 GHz exposure data from this study into the existing knowledge base will help establish damage thresholds in the 6–300 GHz band. The distinguishing factor for RF exposures in this GHz band is that the exposures only superficially penetrate the skin; and thus, deeper tissues are not directly affected by the RF energy (except the eyes when open). The subsurface tissues may be heated due to conduction from the surface, but the effect is purely thermal, and any physiological impact to those tissues can be determined by the existing medical knowledge on burns and hyperthermia. Thus, defining damage thresholds for RF exposures in the 6–300 GHz band should only require knowledge of damage to the skin and eyes from these exposures. Damage to the eyes from RF exposures in this band has been studied previously (Chalfin *et al* 2002, Kojima *et al* 2009, Parker *et al* 2020, Foster, Laakso & Chalfin 2021); and thus, the focus of this study will be the skin.

To generate hazard data for skin, our laboratory conducted two similar studies involving microwave exposures at 8.2 and 95 GHz, with incident fields of 4–30 W/cm^2 and 2–15 W/cm^2, respectively, on swine skin to determine the fluence for burn thresholds. These studies expanded upon the previous burn data generated by our laboratory at lower power densities (2–4 W/cm^2) (Parker *et al* 2021b). The previous study found approximate thresholds for superficial and partial-thickness burns resulting

Accepted Manuscript

from RF exposures at 95 GHz. Since that study was completed, improvements in RF and thermal modeling, dosimetry, instrumentation, and burn characterizations have enabled us to conduct an improved version of the burn study. The improvements will enhance the fidelity of simulations and damage estimates resulting from the exposures. Additionally, because the previous study characterized the superficial and partial-thickness burn thresholds, emphasis was placed in this study on determining the full-thickness burn threshold. The partial-thickness and full-thickness burn thresholds have additional importance, as these thresholds correspond to injury levels where burns are considered a significant injury (Simonds *et al* 2012).

Burn thresholds were obtained from animal models due to the complexity of the burn response at the organism level (Gibson *et al* 2020). Juvenile pigs were selected as an appropriate animal model for the exposures because their skin is the most anatomically similar to human skin (Moritz & Henriques 1947, Montagna & Yun 1964, Meyer *et al* 1978, Sullivan *et al* 2001).

This paper focuses upon the exposure methodology, dosimetry, and histology results from the microwave exposures. Future studies will focus on the effectiveness of non-invasive measurement techniques for predicting burn severity, validation of simulations of RF exposures to the skin, and improvements on dosimetry measurements that help address deficiencies in the characterization of the exposure.

2. Methods and Procedures

2.1. Animal Use

Twenty-two pigs (*Sus scrofa*, Yorkshire, female, ages and weights shown in table 1) were used in this study. Six were used in pilot studies, and the remaining sixteen were divided into two groups of eight swine each for the main studies at 8.2 and 95 GHz. Animals had access to food and water *ad libitum*, and were allowed to acclimate to the laboratory facilities for at least 7 days prior to exposure.

Table 1. Swine ages and weights

Phase	Avg Age (days)	SD Age (days)	Avg Weight (kg)	SD Weight (kg)
Pilot	152	16	69.7	11.4
Main 95	130	12	61.2	3.5
Main 8.2	142	11	56.7	16.5

All ages and weights were recorded on the day of exposure.
SD = standard deviation

The animals involved in this study were procured, maintained, and used according to an IACUC-approved Animal Use Protocol and established animal welfare standards, compliant with: DoD Instruction 3216.01 (2019); US Department of Agriculture Animal Welfare Regulations (2022); The Guide for the Care and Use of Laboratory Animals,

Accepted Manuscript

8th Edition, (National Research Council 2011); and DHA-MSR 6025.02 (Defense Health Agency 2022). The Air Force Research Laboratory at Joint Base San Antonio (JBSA) Fort Sam Houston, Texas has been accredited by AAALAC International since 1967.

2.2. Analgesia and Anesthesia

Prior to waxing, analgesia was administered preemptively with Buprenex (0.007 mg/kg, subcutaneous (SQ)) in the lateral neck. Similarly, prior to the RF exposures, Buprenorphine SR-Lab (0.24 mg/kg, SQ) was administered preemptively in the same location. Throughout the course of the experiment, the animals were monitored each day for indications of pain. If there were changes in behavior or vital signs, the attending veterinarian was notified, and appropriate steps were taken to alleviate the pain. Only one subject exhibited any signs of pain post-exposure, and that subject's pain was alleviated by an additional dose of Buprenorphine SR-Lab.

Prior to anesthesia on the day of exposure, the animal was induced with an injection of tiletamine-zolazepam (Telazol, 4–6 mg/kg, intramuscular (IM)) and anesthetized initially with 3–5% isoflurane in oxygen via a facemask. The pig was then intubated with an endotracheal tube and placed on an automatic ventilator with the initial tidal volume at 8–12 ml/kg, peak pressure at 20 cm H_2O, and respiration rate at 8–20 breaths per minute. The ventilator setting was adjusted to maintain an end tidal PCO_2 of 40±5 mm Hg. Anesthesia was maintained with 1–3% isoflurane in oxygen. Also, since isoflurane was used for an extended period of time (> 1 hr), maintenance fluids (10–15 ml/kg/hr) were administered. Throughout the course of the procedures, vital signs were continuously monitored and kept constant by adjusting the isoflurane dose and using warming blankets and underbody pads. On Days 1, 3, and 7 post-exposure, and on waxing day (3–4 days pre-exposure), the animals were briefly anesthetized to obtain images and biopsies (post-exposure) or remove hair (pre-exposure). On these days, the animals were sedated with tiletamine-zolazepam (Telazol, 4–6 mg/kg, IM) and maintained under anesthesia (3–5% isoflurane) via mask.

2.3. Experimental Setup

All RF exposures were conducted in enclosed, RF-absorbing, anechoic chambers at the Tri-Service Research Laboratory, JBSA Fort Sam Houston, TX. The 95 GHz MMW exposures used a pulsed 1 kW, adjustable pulse repetition frequency (PRF), coupled-cavity, traveling wave tube (CCTWT) source. The 8.2 GHz exposures used a 20 kW, continuous wave, klystron transmitter (Model 6740, Cober Electronics, Connecticut). For both sources, the RF energy was transmitted through a rectangular waveguide (WR-10 for 95 GHz and WR-112 for 8.2 GHz) terminated by a pyramidal horn and into the chamber. The RF beam emitted by the horn passed through a custom-built, dielectric lens (Sheldon 1991), which focused the energy to a 1.7 cm full-width at half-maximum (FWHM), Gaussian spot for 95 GHz and 10.0 cm FWHM for 8.2 GHz. The spot size

Accepted Manuscript

was larger at the lower frequency due to the difference in the wavelengths of the RF energy.

The experimental apparatus used to conduct all of the exposures is shown in figure 1. The anesthetized pig was lying prone with the legs extended away from the body, and the first exposure site positioned at a fixed distance from the transmitter. The distance to the exposure site was verified before each exposure through the use of two laser pointers that intersected at the desired distance from the transmitter (261 cm for 95 GHz and 130 cm for 8.2 GHz). One laser pointer was placed at the lens center and aligned to the beam centerline so that it would minimally interfere with the MMW beam. The second laser pointer was placed on an optical mount, 120 cm off centerline. The pig was placed on a surgical table that could move the pig vertically, horizontally, and rotate about its longitudinal axis to align the exposure site normal to the beam. An infrared (IR) camera (SC6700, Teledyne FLIR LLC, Wilsonville, OR) was placed on a tripod at beam height at a set distance from the subject (60 cm for 95 GHz, 80 cm for 8.2 GHz). The additional camera standoff at 8.2 GHz was required to reduce reflections from the larger beam size. The IR camera was remotely controlled by a networked computer (not shown), which synchronized the camera with the transmitter and also stored the IR video during the data collection phases.

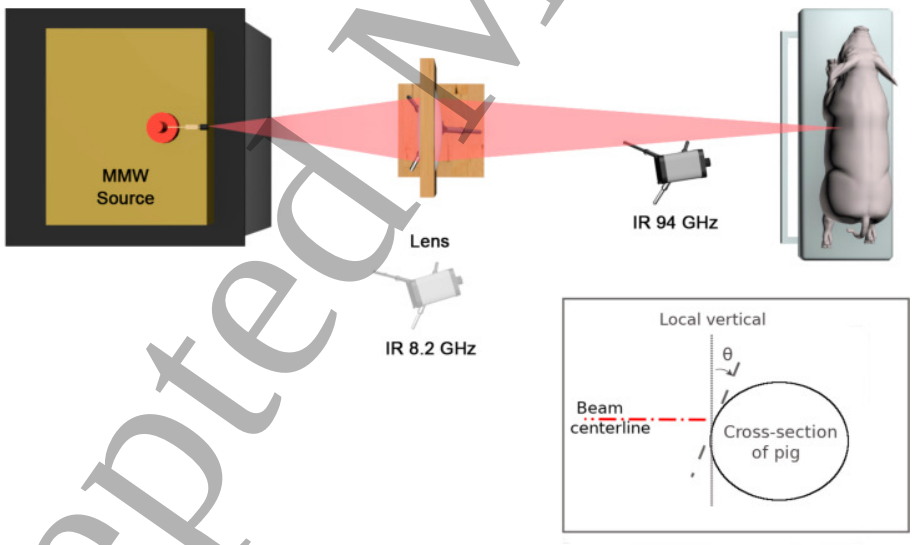

Figure 1. Experimental setup. Main beam of the transmitter is shown in red. The IR camera for the 8.2 GHz exposures is semi-transparent to indicate the new position for those exposures. The insert at the lower right graphically defines θ, which represents the angle between local vertical and the plane tangent to the point of the pig flank directly on the beam centerline. The curved arrow indicates the direction of positive increases in θ.

For each exposure, the subject was positioned to align the exposure site as normal to the beam as possible. Due to the natural convexity of the swine's flank, the site was not normal, so a digital level (AngleCube, iGaging, San Clemente, CA) was used to measure the angle of the skin ($\pm$ 0.5°) relative to local vertical (θ, see figure 1).

Accepted Manuscript

Once positioned appropriately, the site was irradiated using the appropriate source at the desired power density for 5 s. Sham or positive control sites were positioned at the beam centerline, but the transmitter was not energized. After exposure, the subject was positioned for the next site. Once all sites were complete, the subject was returned to the vivarium laboratory, where the positive control exposures, post-exposure imagery, and biopsies were conducted. All trials for a subject (RF + positive controls + shams) were completed within a 40 and 100 min time frame for the 8.2 and 95 GHz exposures, respectively.

2.4. Dosimetry

Measurements of the 95 GHz field intensity were made using two complementary methods: RF power meter and thermal rise of a calibrated, flat plate. The RF power meter method involved the use of a diode power sensor (HP-W8486A, Hewlett-Packard, Palo Alto, CA) coupled to an open-ended, 95 GHz waveguide section, and a power meter (HP 438A, Hewlett-Packard, Palo Alto, CA) is used to display the output. The sensor was mounted on a six-axis robotic arm (VS068A4-AV-6-NNN, Denso Wave, Inc., Aichi, Japan) to accurately scan across the exposure region at millimeter resolution. A calibrated sheet of 15% carbon-loaded Teflon (CLT) (Polytetrafluoroethylene) was placed normal to the beam 261 cm from the transmitter (the desired exposure distance) to verify the power density and beam diameter in accordance with the method described in Parker *et al* (2021a). The RF power meter was NIST traceable (which sets the measurement standard at 95 GHz at ± 1 dB), and the CLT sheet method was within 2.2% of the power meter. Power output of the transmitter was regulated by the use of computer-controlled variations in the duty cycle of a 1 kHz rectangular pulse train that gated the output of the transmitter oscillator.

Measurements of the 8.2 GHz field intensity were made using a broadband electric field probe (EP-602, Narda, Milan, Italy). The same robotic arm was used to accurately position the probe in the exposure region. Power output of the transmitter was regulated by a computer-controlled, analog signal generator (E8247, Keysight Technologies, Colorado Springs, CO) to supply the input voltage to the transmitter. Additionally, transmitter output power was monitored with a diode power sensor (HP-W8481H, Hewlett-Packard, Palo Alto, CA) connected to a directional coupler mounted before the output horn, with a power meter (HP 437B, Hewlett-Packard, Palo Alto, CA) used to display the output. The beam shape was estimated from the heating patterns resulting from 0.3 s, 10 W pulses on a thin plastic sheet using the IR camera.

2.5. Imaging Burn Sites

Digital, color photos were collected at each of the 5 experimental time points (pre-, 1 hr post-, 24 hr post-, 72 hr post-, and 7 days post-exposure). A large scale photo of the entire pig flank and smaller scale photos of each exposure site were collected. A standardizing color map (Tiffen Gray Scale, Tiffen Company, Hauppauge, NY) and two

Accepted Manuscript

rulers were included in each photo to account for differences in illumination and camera orientation.

During the exposures, IR thermography was collected at each site with the IR camera for 0.5 s before the exposure until 1–30 s post-exposure, the variation due to extraneous factors. The camera uses a 640×512 sensor array with closed cycle cooling to allow the images to be internally calibrated. IR thermography images were collected at 125 fps, and the pixel resolution was 24.0 or 32.3 pixels/cm for the 8.2 or 95 GHz exposures, respectively. Prior to each exposure session, a two-point, non-uniformity correction was conducted using a black-body source (Mikron M345, Micron Infrared, Inc., Oakland, NJ). As the temperature range of the exposures spanned 25–115 °C, operating the IR camera in superframing mode was necessary to collect data over the entire range. The two temperature spans used for the superframing mode were 10–90 °C and 50–150 °C. Using this mode reduced the effective frame rate to be 62.5 fps, as the camera interleaved the frames associated with the two temperature calibration settings. Superframing was not used for the first pig in the 95 GHz main study, which caused the temperature readings to saturate for the 12 and 15 W/cm^2 conditions.

2.6. Linking biopsy sites to IR imagery

Because exposures in this study could be at low levels or required biopsy punches along 95% and 50% thermal contours, the intended biopsy sites were not visually distinct. This created a problem to determine where a biopsy should be collected. The solution was to review the IR imagery collected during the exposure and note the pixel positions of the corners of the box surrounding the exposure. Then, measurements of the positions of the appropriate grid box were made at the time of the biopsy. Neither the IR imagery nor skin measurements were exactly 5×5 cm due to the stretching and relaxation of the skin resulting from differences in the body position of the subject compared to when it was marked on Day 0. Additionally, the IR camera view angle was not normal to the site; and thus, the IR image required a correction for perspective. By determining an affine transformation that mapped the positions of the corners in the perspective corrected IR image to the current positions on the pig skin, appropriate positions for biopsy punches were determined (see figure 2).

2.7. 95 GHz Exposures

A pilot study involving five (N=5) pigs spanning the power densities 1.5–40 W/cm^2 were used to establish the exposure conditions for the main study. The main study involved eight pigs (N=8) exposed for 5 s at power densities of 2–15 W/cm^2 using a 1.7 cm FWHM Gaussian spot size. A listing of all exposures for the pilot and main study are provided in the Supplemental Information tables S1–S15. Three or four days prior to the exposure, each pig was sedated and a region was selected that was at least 40 cm long × 10 cm wide along each flank, more than 3 cm laterally from the spine, and between joints of the fore- and hind-legs. The hair within this area was removed using a commercial

Accepted Manuscript

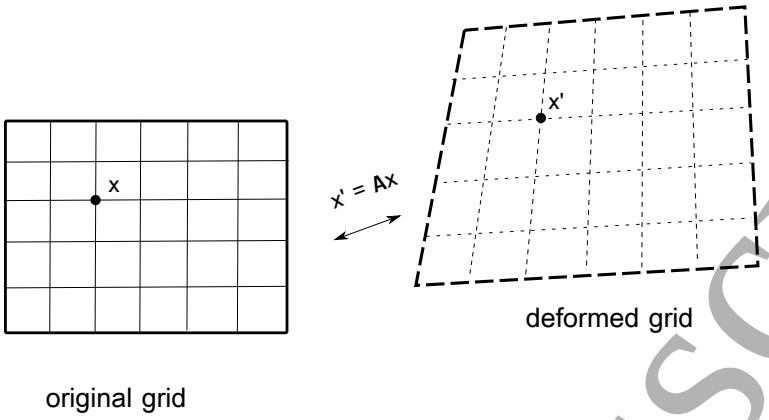

Figure 2. A reversible mapping of points on the skin with the IR imagery was determined using an affine transformation based on registration of the corner points. The skin surface was distorted due to differences in the position of the pig.

hair removal waxing product, and then disinfected with chlorhexidine and/or soap. On the exposure day (Day 0), the pigs were sedated for the duration of all procedures and exposures. First, any hair regrowth in the waxed region was removed with a razor. Then, 2×8 grids, where each grid is 5×5 cm, were drawn onto each flank (32 sites total) using a ruler and permanent black marker, and then, a silver-inked marker was used to mark each corner position in the grid. The silver marker provided better contrast on the IR imagery, which helped in the registration of points in the collected IR data. Pre-exposure digital photographs were collected as described in section 2.5. Then the subject was transferred to the exposure chamber, where the experimental setup described in section 2.3 was arranged. The 32 exposures were conducted sequentially in accordance with that subject's exposure matrix, *viz.*, the top row on the left, then bottom row on the left, then top and bottom on the right. IR thermography was collected during this session as described in section 2.5. Upon completion of all 32 exposures, the subject was returned to the vivarium laboratory. There, the positive thermal control exposures were conducted. Brass slugs, 3 cm in diameter and heated to 100.0±5 °C were placed in direct, thermal contact with the skin for a set duration (10 or 13 s) with steady contact pressure maintained by internal spring tension. The positive control exposures were chosen to coincide with similar contact burn exposures conducted by (Burmeister *et al* 2019, Ponticorvo *et al* 2014, Ponticorvo *et al* 2019) that generated partial-thickness burns. After the positive controls were complete, the 1 hr post-exposure imaging session would commence as described in section 2.5. Next, a punch biopsy, 6 mm in diameter, was collected from the center of seven exposure sites associated with each of the seven power density exposure conditions. Additionally, a punch biopsy was collected from each of the two sham and positive control sites. The biopsy tissue was divided into two equal sections using a scalpel with one section fixed in formalin for histopathology and the second section placed in Allprotect tissue reagent (Qiagen, Hilden, Germany) for later analysis. The order of biopsy locations for a given condition were randomized and

Accepted Manuscript

are provided in the exposure matrices for each pig in Supplemental Information tables S3–S15. Once all biopsies were complete, the areas were dressed with Tegraderm and non-adherent gauze, and then covered with a layer of Ioban drape. Then, the subject was moved to its home pen to recover.

For the Day 1, 3, and 7 post-exposure sessions, the subject was sedated, the wounds imaged, and 11 biopsies were collected (7 MMW conditions + 2 sham + 2 positive controls). The biopsies for the four time points for the sham and positive controls were collected from non-overlapping areas in the same 5×5 cm patch of skin, rather than the single, center biopsy collection in the MMW exposed sites. This was possible for the controls because the exposure was uniform rather than the Gaussian distribution of the MMW exposures. Following the biopsies on Day 7, the subject was euthanized. After the euthanasia was confirmed, a strip of skin (approximately 1×5 cm and 1 cm thick) was collected at ten of the sites corresponding to the seven exposure, two positive control, and one sham conditions. The strip was excised as close to the center of the exposure as possible without overlapping the existing punch biopsy site.

Because this study involved low power exposures (2 and 3 W/cm^2) to determine the superficial burn threshold, the skin at those sites often exhibited no visible indication of exposure at the time of the biopsy. As mentioned above, this was problematic for determining where the center of an exposure occurred so that a biopsy could be appropriately collected. Using the affine transformation of the IR imagery, the center of the exposure was determined, and the biopsy punch was performed.

2.8. 8.2 GHz Exposures

Following a similar methodology outlined in the 95 GHz study, a single pig (N=1) was used in a pilot study at 8.2 GHz to determine the exposure conditions that would span the burn severity spectrum from no effect to full-thickness burns. This was followed by the main study involving eight pigs (N=8) to determine burn severity from eight RF exposure conditions. A listing of all exposures for the pilot and main study are provided in the Supplemental Information tables S16–S25. The conduct of the exposures was similar to the 95 GHz study except that the beam was larger (0.10 m FWHM), and thus 4 sites (only 2 were RF conditions) were exposed on each flank, 8 sites total per pig (see figure 3). Because the sites were larger, two temperature contours, the 95 and 50% temperature contours relative to the peak temperature change, could be determined from the IR data. Since change in temperature is proportional to the absorbed power density (Foster *et al* 1978), the two contours could be associated with two different power densities. Thus, each exposure site on the pig yielded burn data for two distinct power density conditions. Because the pig flank was not flat, these contour regions were not circular, and had to be correlated with IR imagery to determine the eight biopsy points using an affine transformation. However, the affine transformation did not account for differences in curvature over the flank between the image and the current position. Because a larger region was mapped in the 8.2 GHz exposures compared to the 95 GHz,

Accepted Manuscript

the magnitude of the effect of curvature needed to be quantified. Therefore, each site had two test locations that were used for uncertainty quantification of the accuracy in the transformation.

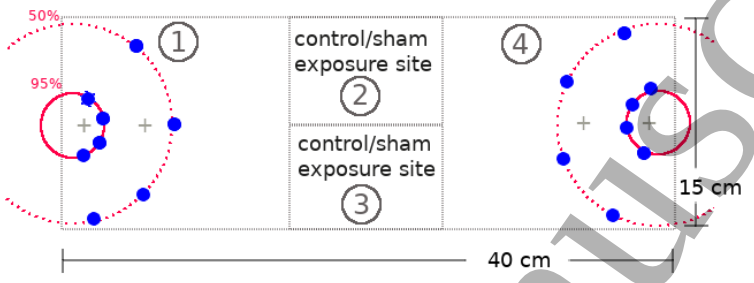

Figure 3. The four exposure sites for the 8.2-GHz study are labeled by numbers within circles. RF beam power and temperature contours are denoted by solid (95%) or dashed (50%), red circles. Notional biopsy points are in blue closed circles. The test locations for the affine transformation are marked with a grey, positive sign (+).

2.9. Histology

Each 6 mm biopsy punch was fixed in 10% neutral buffered formalin for 48 hr, dehydrated in alcohol, and paraffin processed. The resulting paraffin block was then sectioned into 7 μm thick samples, and stained with hematoxylin and eosin (H&E). The slides were reviewed by a board-certified pathologist, who was blinded to the exposure conditions, and scored according to a 20 factor, ordinal point scale created by Gibson *et al* (2020). Because the hairs were removed from the MMW exposed surface by waxing, local inflammation of the hair follicle region was evident in the H&E stained slides at all time points. This artifact required the pathologist to exclude the regions local to hair follicles from his assessment of the skin damage. Since each slide only contained 1–2 follicles, most of the slide area was available for evaluation (see figure 4). Additionally, if in the pathologist's opinion the slide preparation was poor or unacceptable, the data associated with those slides was excluded from further analysis. Burn severity was largely determined from the scores associated with two factors: epidermal and dermal injury scores, using the decision tree in table 2.

Burn wounds are classified based on the deepest tissue damaged as superficial, partial-thickness, or full-thickness, which determines the wound management necessary for successful healing. Superficial burn injuries only involve the epidermis and will heal without medical intervention. Deep partial-thickness burns injure the epidermis and papillary dermis requiring debridement of the necrotic tissue and application of a topical burn dressing (Stone *et al* 2018). Based on Gibson *et al*, losing more than 75% of

Accepted Manuscript

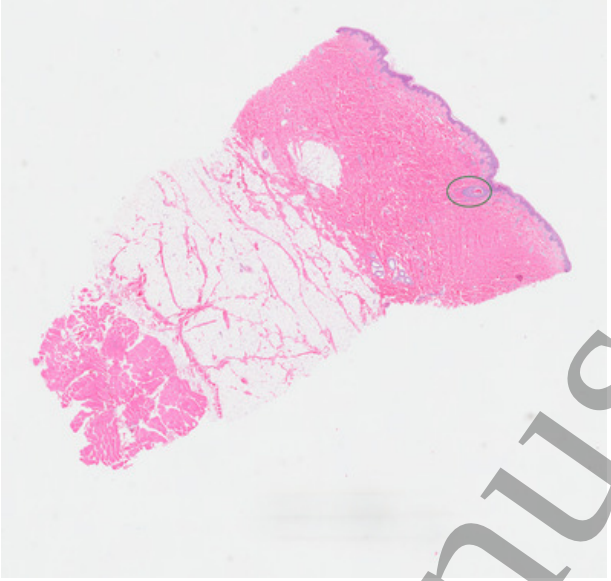

Figure 4. Sample of H&E stained slide demonstrating the relative sizes of the hair follicle to the overall slide. The green ellipse represents the region excluded by the pathologist for damage evaluation.

Table 2. Classification of burn severity based upon histology scores for Epidermal and Dermal injury.

Severity	Epidermal Injury	Dermal Injury	Vascular Occlusion	Adnexal Necrosis
No Burn	0	0		
Superficial	≥1	0		
Partial-thickness	≥3	≥1		
Full-thickness	NA	4/5*	≥4/NA	≥4/NA

*If dermal injury is a 4, then both the vascular occlusion and adnexal necrosis scores must be 4 or more to be classified as full-thickness. If dermal injury is a 5, then the burn is classified as full-thickness.
NA = not applicable

the viability in the tissue, including the reticular dermis and adnexal structures (score 4 or greater) is clinically considered a full-thickness injury that requires surgical excision of the necrotic tissue followed by skin grafting to avoid complications (i.e., hypertrophic scaring) associated with prolonged wound healing.

2.10. Exposure Simulation

A one-dimensional (1D) layered, thermally isolated (adiabatic boundary condition), computational phantom of the skin was used to simulate the thermal response expected from the RF exposures. The layers consisted of epidermis, dermis, fat, and a terminating muscle layer, assumed infinite. These simulations were based upon an analytical solution to Maxwell's equations in 1D coupled to a numerical solution to the Pennes' bioheat equation similar to other studies (Alekseev *et al* 2005, Foster *et al* 2020, Christ *et al* 2020). Briefly, we computed the RF energy deposition from a planewave source

Accepted Manuscript

incident on the layered model by solving the boundary-value problem dictated by Maxwell's equations. This source term was used in a finite-difference solver of the bioheat equation, given by

$$\rho c_p \frac{\partial T}{\partial t} = \frac{\partial}{\partial z}\left(k\frac{\partial T}{\partial z}\right) + Q(z) + \beta\rho_B c_B(T - T_B), \quad (1)$$

where T denotes the temperature, ρ is the density of the tissue, c_p is the heat capacity, k is the thermal conductivity, $Q(z)$ is the source term given by $Q(z) = \rho\text{SAR}$, where SAR is the specific absorption rate, β is the tissue perfusion rate,$\rho_B c_B$ is the volumetric heat capacity of blood, and T_B is the temperature of the core body blood pool, assumed constant. Given the localized nature and short duration of the GHz exposures, we neglect a metabolic heat generation term in equation 1.

Here, similar to (Alekseev *et al* 2005), the temperature history (heating and cooling phases) from three exposures during the pilot studies at 8.2 and 95 GHz were used to determine an effective thermal conductivity in the epidermis and dermis (0.5 W/m/ °C) and a dermal perfusion rate (2.0×10^{-3} ml/s/ml) that was used for all simulations. All subsequent analyses make use of this thermal conductivity and perfusion rate. All other dielectric and thermal properties were taken from the IT'IS database (Hasgall *et al* 2018). The thicknesses of the layers were based upon biopsy data from Yorkshire pig flanks (Vincelette *et al* 2012).

Using the perfusion and conductivity values determined from the pilot data, the simulated temperature response from a 1 W/cm^2 exposure of the 1D layered phantom was linearly scaled to fit the heating profile of a patch of skin associated with the hottest pixel to provide an estimate of the peak power density for each trial, which should correspond to the center of the Gaussian beam. Each fit was constrained to a single free parameter, the power density on target. Because the relative temperature data is accurate within 20 mK and is independent of the RF power meters, these calculations provided a measure of the variation in the absorbed power due to experimental factors for each trial.

3. Results

3.1. Temperature Correlations

Figures 5 and 6 show the average surface temperature profiles for the regions associated with the biopsy locations for each RF exposure condition in the 95 and 8.2 GHz studies, respectively. Each time trace represents the average of the temperature readings from pixels associated with the biopsy punch for all skin samples at that RF condition. Error bars represent 1 SD of the data at each time point and RF condition. Some exposures ended prematurely; and therefore, the plots represent statistics from the available data at that timepoint. Figures 7 and 8 represent the distribution of skin temperatures in the region of a punch biopsy for a typical trial at 95 and 8.2 GHz, respectively. In addition, the blue line in each plot represents the 1D model estimate for that exposure. Each

Accepted Manuscript

empirical trace shows the temperature history of the min, 5% quantile, 25% quantile, median, 75% quantile, 95% quantile, and maximum for the pixels in a region associated with the 6 mm biopsy punch plus any uncertainty in determining the punch location. The 1D model is well correlated to the median temperature rise during the exposure on times, and thus is a good predictor of peak temperature. The cooling phase is well represented in the 95 GHz case, but less so for 8.2 GHz. The Supplemental Information contains an HDF archive (The HDF Group & Koziol 2020) with these same temperature distributions for every trial in this study, except where IR data was not available due to camera malfunctions.

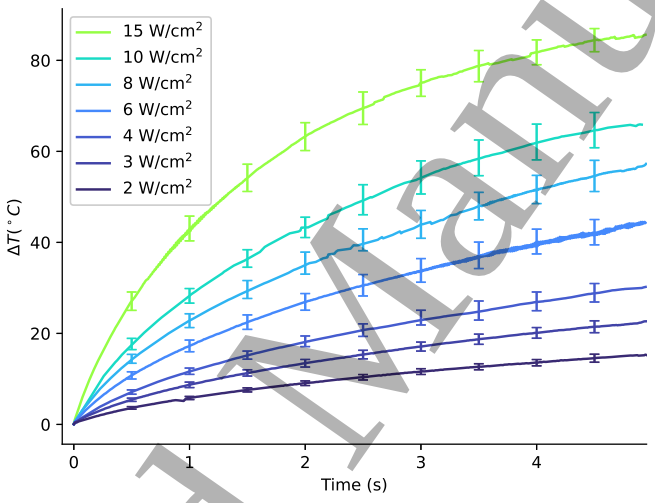

Figure 5. Mean change in surface temperature versus time for each 95 GHz exposure condition at the biopsy site. Error bars represent 1 SD. Colors are assigned from a sequential colormap to each power density.

In figure 9, the power densities determined from dosimetry measurements for 8.2 and 95 GHz exposures were compared to the predicted power density using the 1D, layered computational phantom. The triangles and circles represent the estimated, normalized power densities for 8.2 and 95 GHz exposures, respectively. The data points for the 8.2 GHz, 8 W/cm^2 condition are shifted to the right to avoid overlap with the 95 GHz data at the same power density. The error bars represent 1 SD. The power density predicted by the 1D layered phantom was computed from the least-squared fit of the temperature history for each trial and corrected using Fresnel's equations for angle of incidence by $1/\cos^2(\theta)$ (Jackson 1999). As expected, large angles of incidence ($> 10°$) did affect the absorbed RF energy, which can be seen in a similar plot in the Supplemental Information that does not correct for θ. Averaged over all conditions, the 1D model underestimated the measured power densities by 4%, which is probably indicative of the fact that the single measure of the incident angle at the center of the exposure was not sufficient to account for the curvature of the skin over the exposure site. The convex curvature reduces the absorbed RF energy leading to lower skin

Accepted Manuscript

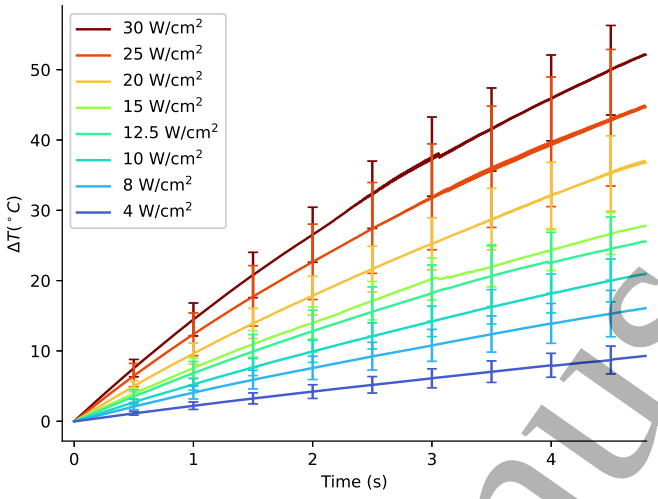

Figure 6. Mean change in surface temperature versus time for each 8.2 GHz exposure condition at the biopsy site. Error bars represent 1 SD. Colors are assigned to each power density using the same sequential colormap as in figure 5. Nominal power densities were 8, 20, 25, and 30 W/cm^2 with punch biopsies taken at the 95% and 50% contours.

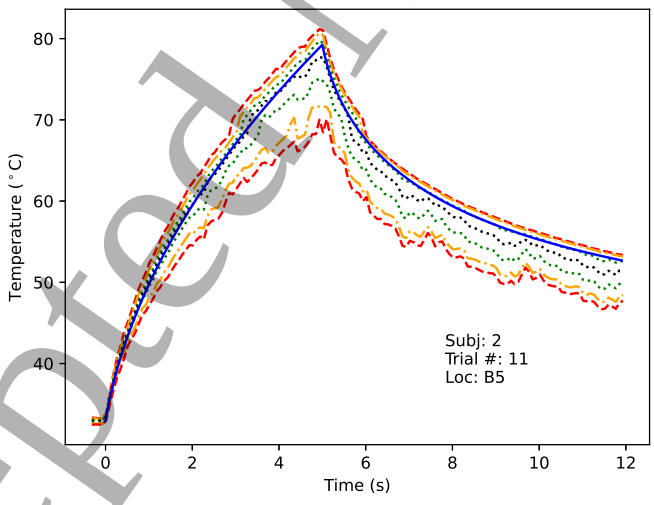

Figure 7. Distribution of temperatures over the biopsy region for a representative 95 GHz exposure. The solid line represents the median temperature over the region, the green, dotted lines represent the 25% and 75% quantiles, the yellow, dashed-dotted lines represent the 5% and 95% quantiles, and the red, dashed lines represent the minimum and maximum temperatures. The solid, blue line represents the estimated temperature from the 1D model.

temperatures than would be expected from measurements of the free field even after correcting for the central angle relative to the beam path. Since the power density from

Accepted Manuscript

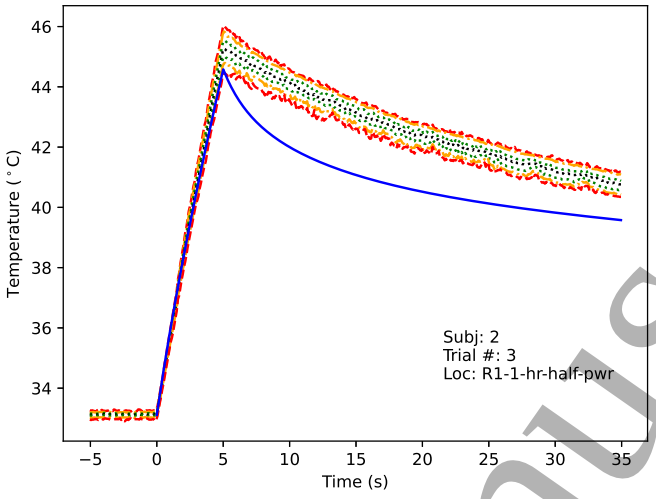

Figure 8. Distribution of temperatures over the biopsy region including uncertainty in registration of IR data points for a representative 8.2 GHz exposure. The dotted, black line represents the median temperature over the region, the green, dotted lines represent the 25% and 75% quantiles, the yellow, dashed-dotted lines represent the 5% and 95% quantiles, and the red, dashed lines represent the minimum and maximum temperatures. The solid, blue line represents the estimated temperature from the 1D model.

the 1D phantom resulted from the fit of the observed temperature profile, the lower modeled power density results provide an estimate of the effect curvature would have on the exposures in this geometry.

3.2. Histopathology Results

Standard box plots representing the histological scoring of epidermal and dermal burn depth for all exposures at 95 and 8.2 GHz are shown in figures 10–13. The median is represented by a thick horizontal, grey line in the box, and the whiskers extend to the lesser of 1.5× the inner quartile range or the minimum and maximum values for that condition. Because the data is ordinal, a small amount of jitter was added horizontally to each data point to allow an estimate of the number of responses at a given condition. The four plots represent the extent of the damaged tissue in the epidermis and dermis, respectively, according to the 0–5 scale shown in table 3.

The box plots demonstrate that the RF exposures behave in a dose-dependent manner, i.e., the injury severity increases as the energy deposited increases. Additionally, there are threshold levels, below which the severity is consistently low; then near threshold, the severity spans the full range of severity scores due to variability in subjects and exposure; and lastly, suprathreshold exposures that are consistently high, but have more variability than the below threshold exposures again due to subject and exposure variability. One difference in the severity between the 8.2 GHz exposures

Accepted Manuscript

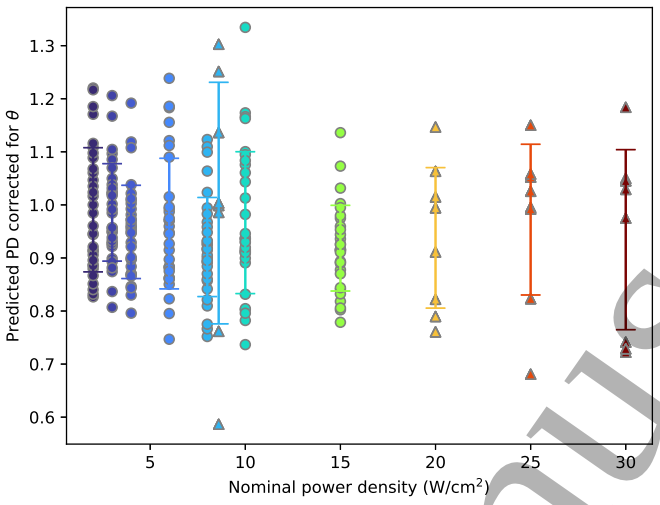

Figure 9. Comparison of empirically measured power densities to the predicted values from the 1D layered, computational phantom. Triangle markers indicate 8.2 GHz exposures, and circles indicate 95 GHz exposures. Error bars represent 1 SD of the predicted values. Colors are assigned to each power density based on the same colormap in figure 6.

Table 3. Severity scores for histology assessment of burn depth in epidermal and dermal layers of skin.

Score	Description
0	Normal tissue
1	Damage extends through 0–25% of the layer
2	Damage extends through 25–50% of the layer
3	Damage extends through 50–75% of the layer
4	Damage extends through 75–99% of the layer
5	Damage extends through 100% of the layer

and the 95 GHz exposures is that the transition between superficial burns to more severe partial thickness or full thickness burns occurs quicker (over a smaller range of power density changes) for 8.2 GHz than the 95 GHz exposures. Specifically, the severity for 95 GHz exposures gradually increases over the full range of powers explored (2–15 W/cm^2), whereas the 8.2 GHz exposures have a marked change at (10–15 W/cm^2). Below this region the histology scores are essentially 0–1 and above they are 4–5. This effect is assumed to reflect the deeper penetration of the lower frequency MMW energy such that when the temperature is sufficient to damage the surface, the subsurface temperature has been heated to a similar temperature by the penetrating energy. These plots also show that 2 out of 123 acceptably prepared, sham exposed samples exhibited damage consistent with superficial burns, which presumably is due to trauma caused by the waxing procedure or histology processing artifacts. Five sham and 23 RF exposed samples (out of a total of 736) were excluded due to poor slide quality. Box plots showing

Accepted Manuscript

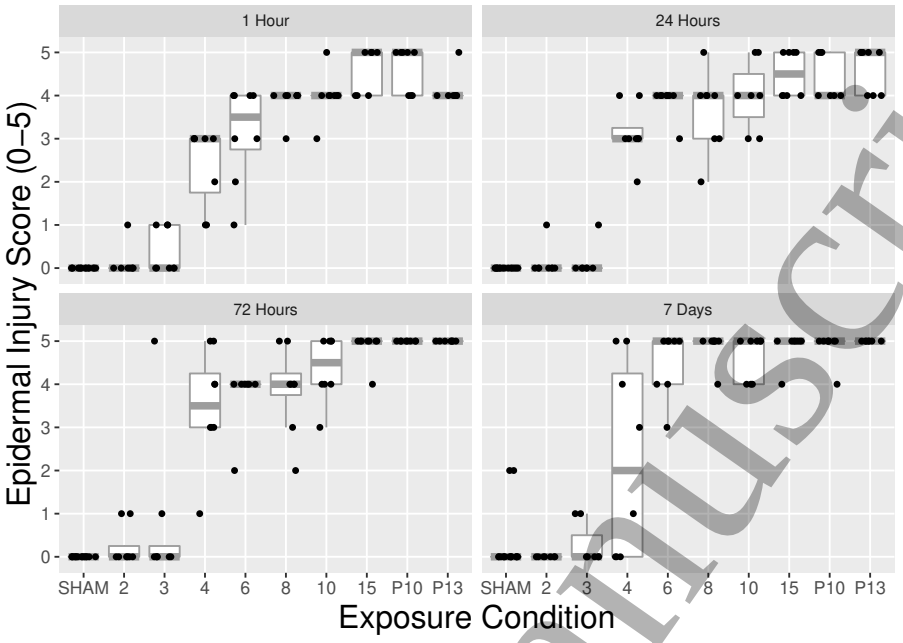

Figure 10. Box plots of the epidermal injury scores for each exposure condition at 95 GHz at each experimental time point. Each exposure condition is listed by the nominal power density in W/cm^2, SHAM for sham exposures, or P10 and P13 for the positive control contact burns for 10 and 13 s, respectively. Jitter was added to each data point to visualize the number of responses at a given condition.

the scoring of the other 18 histopathology categories defined in Gibson *et al* (2020) for all exposures at 95 and 8.2 GHz are shown in the Supplemental Information.

3.3. Damage Modeling

Two traditional damage metrics were computed for these burn trials: CEM_{43} and Arrhenius, and each was compared to the histological assessments of severity. The CEM_{43} metric was computed for the mean thermal response of each RF condition and compared to the associated burn severity level for each trial at that condition. The results are shown in table 4, where the values associated with the burn severity are the number of observations of that burn severity found in the histology for that RF condition, and the CEM_{43} value is computed from

$$\mathrm{CEM}_{43} = \int dt\ R^{(43-T(t))}, \tag{2}$$

where $T(t)$ is the temperature (in °C) at time t for the mean responses shown in figures 5 and 6. The last column in table 4 computes the ratio of the experimental exposure to the exposure reference level (ERL) for restricted environments in the IEEE C95.1-2019 standard (IEEE 2019).

The first feature to observe from table 4 is that as expected the transition from healthy to damaged tissue (burns) are associated with CEM_{43} values of 10-100 (van Rhoon *et al* 2013). Additionally, the CEM_{43} values for the 95 GHz exposures ≥ 6W/cm^2

Accepted Manuscript

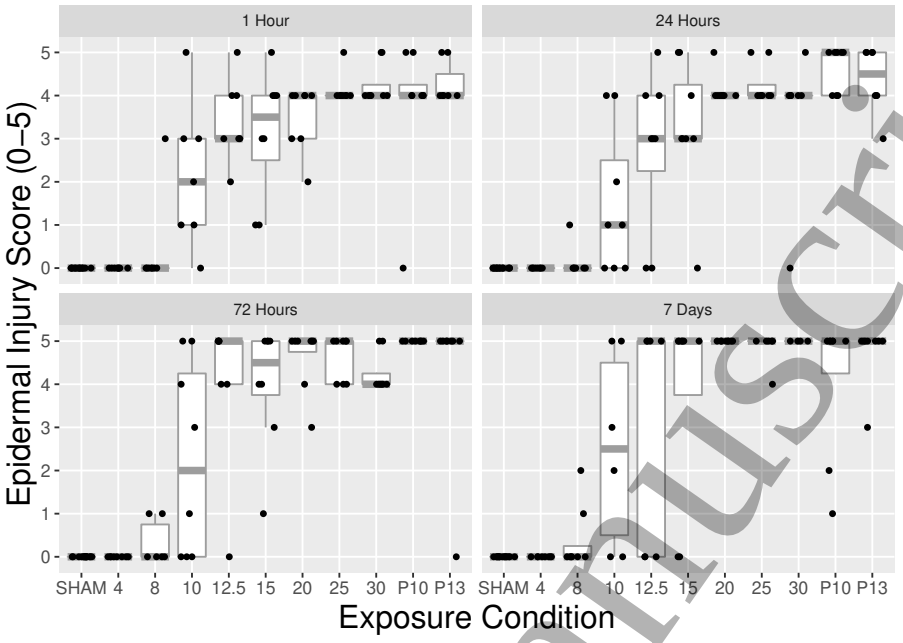

Figure 11. Box plots of the epidermal injury scores for each exposure condition at 8.2 GHz at each experimental time point. Each exposure condition is listed by the nominal power density in W/cm^2, SHAM for sham exposures, or P10 and P13 for the positive control contact burns for 10 and 13 s, respectively. Jitter was added to each data point to visualize the number of responses at a given condition.

are many orders of magnitude above the 8.2 GHz exposures ≥ 20 W/cm^2, yet the severity of the 95 GHz burns are essentially limited to partial thickness burns compared to the full thickness burns at 8.2 GHz. Hence, there is poor correlation of burn severity with the CEM_{43} values. This is partially explained by the dependence of CEM_{43} values on surface temperatures, while burns involve damage to subsurface tissues and possible inaccuracy of the CEM_{43} metric at high temperatures (> 55 °C) (Dewhirst *et al* 2003). Of note, the maximum temperatures for the 10 and 15 W/cm^2 conditions at 95 GHz exceeded 100 °C, which is consistent with the blistering that manifested with these exposures. However, the temperature reported is based upon IR data. Since the IR emissivity of the steam is slightly lower than the 0.98 value used for skin, the actual temperature may be slightly higher. The 95 GHz exposures have significantly higher safety factors due to the introduction of the fluence limits for exposures above 30 GHz. The 8.2 GHz exposures at 10–15 W/cm^2 were less than 10× the IEEE limit, yet they resulted in partial thickness and full thickness burns. The higher power (≥ 20 W/cm^2) 8.2 GHz exposures largely resulted in full thickness burns at levels that were 15–20× the IEEE limit.

Next, using the Arrhenius integral based procedure that associates the burn depth with the deepest tissue layer that yields an Arrhenius damage integral equal to one ($\Omega = 1$) (Knox *et al* 1979), an estimate of the burn depth from the 1D layered phantom is made for every trial. The Arrhenius values for the rate constants were acquired from

Accepted Manuscript

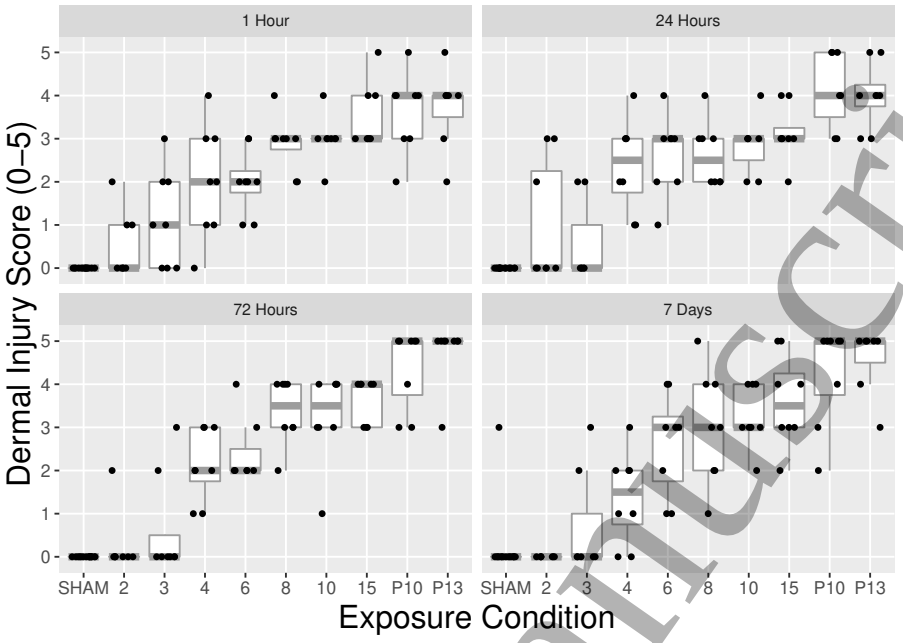

Figure 12. Box plots of the dermal injury scores for each exposure condition at 95 GHz at each experimental time point. Each exposure condition is listed by the nominal power density in W/cm^2, SHAM for sham exposures, or P10 and P13 for the positive control contact burns for 10 and 13 s, respectively. Jitter was added to each data point to visualize the number of responses at a given condition.

Pearce (2009) and are listed in table 5. The model predicted burn depths for each trial are paired with empirical burn severity levels that are assigned by converting the 20-factor, histology score for each trial using table 2, and the results are presented in figure 14. The dashed, vertical lines denote the boundaries of the epidermis and dermis in the 1D phantom (at 80 and 2780 μm, respectively), and the colored bands provide visual guides for the regions associated with each histologically determined, burn severity level.

The lines and colored bands break up the domain into boxed regions. If one adds a region associated with just the surface (zero depth), then ideally, the plot would have a block-diagonal shape, e.g., all of the exposures associated with the "partial-thickness" condition should have a burn depth in the dermis (80–2780 μm). The majority of points do follow this trend, which supports the use of the 1D model to predict burn severity.

Where there were disparities of the ideal block-diagonal shape of histology assessments and predicted burn depths, the probable causes were a) accuracy of the registration of points in the IR video with the biopsy centers, b) differences in the actual thickness of the layers for each subject, c) dielectric and thermal properties associated with each tissue, d) cooling differences between biopsy samples taken at the 50 and 95% temperature contours, and e) curvature of the flank at the biopsy position. An indicator of the problems in registration is seen by data points associated with exposures in the lower right that predicted deep burn depths, but histology assessed as "No burn."

Accepted Manuscript

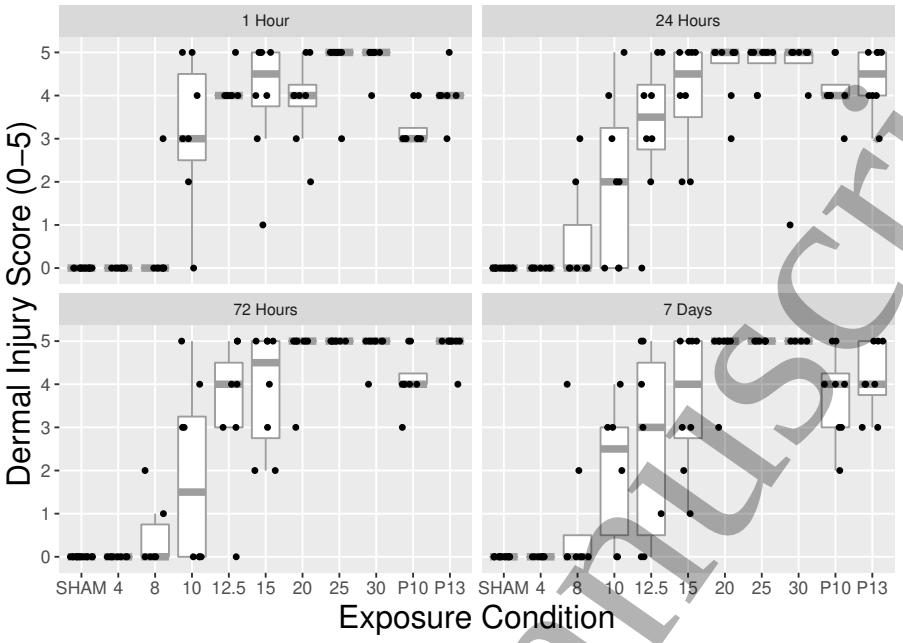

Figure 13. Box plots of the dermal injury scores for each exposure condition at 8.2 GHz at each experimental time point. Each exposure condition is listed by the nominal power density in W/cm^2, SHAM for sham exposures, or P10 and P13 for the positive control contact burns for 10 and 13 s, respectively. Jitter was added to each data point to visualize the number of responses at a given condition.

The IR imagery of that site observed high temperatures that generated the deep burn estimate, but the punch was collected in a presumably different, cooler area. Only 1 data point from the 95 GHz study is found in this errant region because determining the punch site for the 95 GHz samples was easier due to a single punch being made in the center of a smaller region as compared to the multiple measurements that were necessary to find the punch site at 8.2 GHz. The effect of the registration concerns can also be seen in table 4, where 2 exposures at 30 W/cm^2 yielded "no burn", yet the other 30 exposures at that level were significant burns. Improvements on measuring the curvature of the flank and integrating that information in the registration of the biopsy points could reduce the positional uncertainty, which would provide a better estimate of the temperature history associated with a biopsy.

The variation in the layer thicknesses for each individual will have a stronger effect on the temperature response at 8.2 GHz due to the deeper penetration depth, which will also tend to cause a larger uncertainty in the 8.2 GHz data. The 1D model also cannot account for the spatial temperature gradient at the 50% power biopsy sites, which could affect the time history of the surrounding tissue and hence the damage observed. It should also be noted that the 2 sham exposures that exhibited damage (see figure 10) had histology scores that would be consistent with superficial burns (epithelial damage less than 100% thickness), which could indicate that all samples have potentially higher histology scores due to artifacts related to waxing and sample preparation.

Accepted Manuscript

Table 4. CEM_{43} values, burn severity, IEEE safety margins associated with mean response of each RF condition

Freq (GHz)	Power Density (W/cm^2)	max T (°C)	No	S	PT	FT	CEM_{43} (min)	safety factor
8.2	4	41	32	0	0	0	5×10^{-4}	3
8.2	8	48	26	5	1	0	3×10^{-1}	6
8.2	10	53	10	10	11	1	9×10^{0}	7
8.2	12.5	58	9	1	19	3	2×10^{2}	9
8.2	15	60	2	3	18	9	9×10^{2}	11
8.2	20	69	0	1	15	16	3×10^{5}	15
8.2	25	77	0	0	8	24	8×10^{7}	18
8.2	30	85	2	0	4	26	2×10^{10}	22
95	2	48	27	5	0	0	3×10^{-1}	45
95	3	55	22	7	2	0	4×10^{1}	67
95	4	63	3	6	23	0	6×10^{3}	90
95	6	77	0	3	27	1	8×10^{7}	130
95	8	90	0	2	30	0	5×10^{11}	180
95	10	100	0	0	32	0	4×10^{14}	220
95	15	118	0	0	28	2	3×10^{20}	340

No = No burn
S = superficial burn
PT = partial thickness burn
FT = full thickness burn

Table 5. Kinetic coefficients for skin thermal damage

$A(s^{-1})$	E_a (J/mol)	Temperature region
8.82×10^{94}	6.03×10^{5}	T$\leq$ 53 °C
1.30×10^{31}	2.04×10^{5}	T > 53 °C

A = pre-exponential factor
E_a = activation energy

During the 95 GHz pilot study, we attempted to determine full-thickness burn thresholds from 1 s duration exposures, but after histological assessment, no samples exhibited full-thickness burns even though RF intensities as high as 40 W/cm^2 were used. The surface temperatures exceeded 90 °C, and in most cases, the skin blistered. However, the superficial absorption depth (corresponding to a power density of $1/e^2$ or 13.5% of the surface level) of 300 μm coupled with the short exposure time and the blood flow in the deep dermis prevented sufficient heat from propagating to the dermis-adipose tissue interface and cause damage through the full thickness of the dermis. This thermodynamic limiting effect of the heat conduction was validated in the 1D layered phantom, which predicted that the maximum temperature rise at 2780 μm below the surface (the approximate depth of the dermis-adipose tissue interface) was less than 0.05 °C. The fact that the subsurface thermal dose can be drastically different than the surface thermal dose further supports the use of Arrhenius integral values at depth

Accepted Manuscript

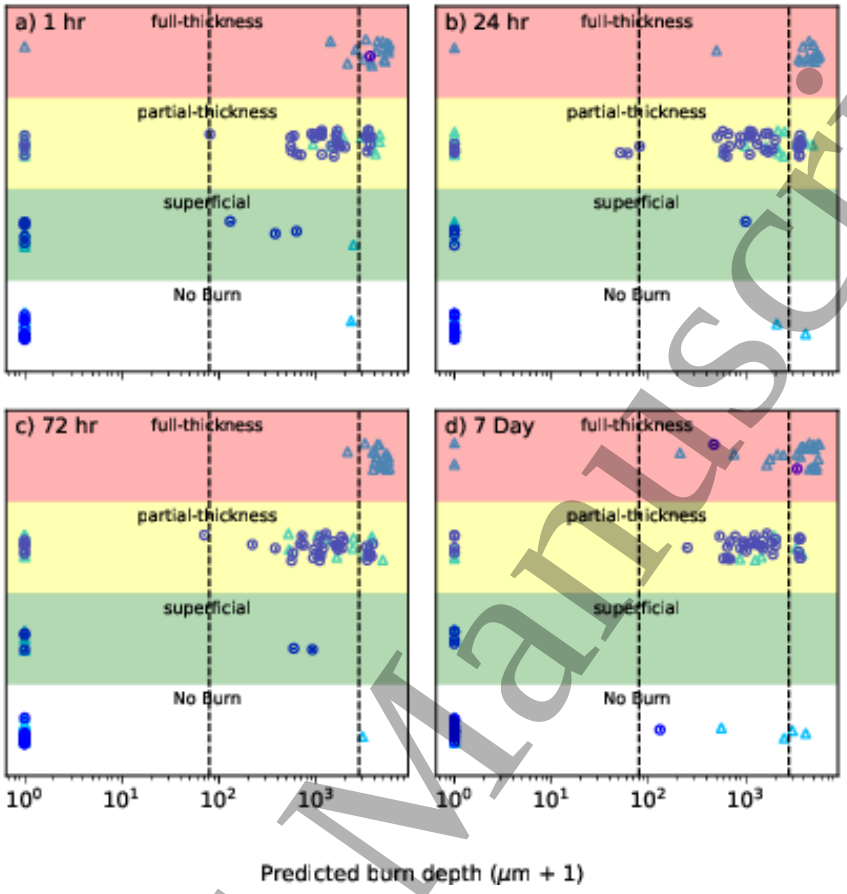

Figure 14. Burn severity associated with each predicted burn depth for the RF exposed samples at all four time points. The triangles and circles represent 8.2 and 95 GHz exposures, respectively. Each of the exposure data points have vertical jitter added to help visualize the number of trials associated with each condition. The dashed, vertical lines indicate boundaries of the epidermis and dermis in the 1D model. The red, yellow, green, and white bands represent regions where the severity of the burn was assessed by histological assessment as full-thickness, partial-thickness, superficial burns, or no burn (normal tissue), respectively. To avoid the logarithm of zero depth, one micron is added to all burn depths.

rather than relying only on surface values (Henriques 1947) to determine burn severity.

4. Discussion

The 2–4 W/cm^2 exposure conditions at 95 GHz were similar to those conducted in Parker *et al* (2021b), where burns were assessed at only 1 time point, Day 3 after exposure and involved multiple durations. For the exposures in the previous study that had 5 s durations, less than 50% of the exposures at 2 W/cm^2 resulted in superficial burns, which compares to 2 of 8 (25%) exposures in this study resulting in epidermal injury scores greater than zero on Day 3 that would be considered superficial burns (see figure 10). More than 50% of the exposures at 3 and 4 W/cm^2 in the previous

Accepted Manuscript

study resulted in partial-thickness burns. For this study, 1 of 8 (3 W/cm^2) and 7 of 8 (4 W/cm^2) exposures resulted in dermal injury scores greater than zero, which would be considered partial-thickness burns (see figure 12). Regardless, as expected the higher power density exposure conditions (6 W/cm^2 and greater) in this study consistently demonstrated higher injury scores than the lower power conditions.

This is the first RF skin burn study at 8.2 GHz that is known to the authors; and thus, there are no empirical data for comparison at these suprathreshold power levels. The 8.2 GHz heating rates compare favorably with the 1D layered model predictions as shown in figure 9. In fact, the high correlation of predicted thermal response with the measured values enhances the confidence in the predictions using the computational phantom.

During the 35 s of IR video collection, subject breathing could cause large relative motion of the skin surface since the camera was fixed. The silver inked points in the corners of the exposure areas were used in a cross-correlation, feature-tracking algorithm to automate the tracking of the skin surface in each trial. The average motion of the four corners was used to determine the center of the biopsy location at each video frame so that appropriate pixels could be extracted from each video. Examples of a temperature history extracted from the IR video with and without the motion artifact removed can be seen in figure S2 in the Supplemental Information, where the maximum difference at a time point is 2.4 °C.

5. Conclusion

In this study, MMW overexposures on swine at two different frequencies were used to determine thresholds for burn damage. At the lower powers where previous data was available, the resulting threshold estimates from this study are in agreement. The higher power exposures demonstrated quicker time to burn estimates than those at lower power. The empirically measured temperature response of the skin across all power densities tested is in agreement with a 1D model of heating that accounts for the conduction of heat during exposure. This model was applied to 352 exposures in this study and the mean response was able to predict 96% of the observed temperature rise (figure 9). There was a standard deviation of 15% associated with these predictions. Additionally, burn depth and severity was found to correlate better with Arrhenius integral values computed at each layer depth using the 1D model than from metrics that use surface values. An extreme case in support of this statement was the observation that 95 GHz exposures at 40 W/cm^2 for 1.25 s did not cause full-thickness burns even though the surface temperatures consistently exceeded 90 °C. The 1D model for that exposure condition estimated the temperature rise at the dermis-adipose boundary to be less than 0.05 °C. The temperature histories and histology results of all swine in the study are available in the Supplemental Information.

Safety factors for exposures used in this study based upon the IEEE C95.1-2019 standard are significantly higher for the 95 GHz exposures compared to 8.2 GHz.

Accepted Manuscript

Exposures at 8.2 GHz that caused at least partial thickness burns were only 7–20× the IEEE limit, which may be of interest since the limit is supposed to be 10× below any significant health effect. At 95 GHz, partial thickness burns were caused at 90× the IEEE limit. For full thickness burns, the safety factor for 8.2 GHz (20–30 W/cm^2) was 15–22x and for 95 GHz (greater than 15 W/cm^2) was greater than 340x. Hence, the safety margins are significantly different over this spread of frequencies. The main contributor to this disparity is that the fluence limit does not apply for exposures less than 30 GHz. Although exposures in the 6–30 GHz band distribute energy over a larger volume of tissue than exposures at $\geq$ 30 GHz, the severity of the injury rapidly changes from superficial to deeper burns with only modest changes in specific absorption. Thus, this study might be of interest to ensure the IEEE safety margins are appropriate in the 6–30 GHz band.

Acknowledgments

The authors gratefully acknowledge the following individuals for providing valuable technical and administrative expertise to the development of this manuscript: Mr. David Fines for animal handling and care, Dr. Benjamin Kalinosky for assistance in the video analysis, Mr. Kevin Mylacraine for developing graphics for some of the figures, Mr. Dave Freeman and Mr. Weston Williams for operation of the 8.2 and 95 GHz transmitters during all phases of the experiment, and Ms. Hilda Hall for editing and formatting.

References

Alekseev S I, Radzievsky A A, Szabo I & Ziskin M C 2005 *Bioelectromagnetics* **26**, 489–501.

Burmeister D M, Ponticorvo A, Yang B, Becerra S C, Choi B, Durkin A J & Christy R J 2019 *Burns* **41**(6), 1242–1252.

Chalfin S, D'Andrea J A, Comeau P D, Belt M E & Hatcher D J 2002 *Health Phys* **83**, 83–90.

Christ A, Samaras T, Neufeld E & Kuster N 2020 *Radiat Prot Dosimetry* **188**(3), 350–360.

Defense Health Agency 2022 'The Care and Use of Animals in DoD Research, Development, Test, and Evaluation (RDT&E) or Training Programs, DHA-MSR 6025.02'.
URL: *https://rt.cto.mil/wp-content/uploads/2019/07/DHA-MSR-6025.02.pdf*

Department of Defense 2019 *Use of Animals in DoD Conducted and Supported Research and Training (DoD Instruction Number 3216.01).*
URL: *https://www.esd.whs.mil/Portals/54/Documents/DD/issuances/dodi/321601p.pdf*

Dewhirst M W, Viglianti B L, Lora-Michiels M, Hoopes P J & Hanson M 2003 *in* T. P Ryan, ed., 'Proc SPIE Int Soc Opt Eng' p. 4954:37.

Foster K R, Kritikos H H & Schwan H P 1978 *IEEE Trans Biomed Eng* **BME-25**(3), 313–316.

Foster K R, Laakso I & Chalfin S 2021 *Health Phys* **120**(5), 525–531.

Foster K R & Vijayalaxmi 2021 *Front Comms Net* **2**, 39.

Foster K R, Ziskin M C & Balzano Q 2021 *Health Phys* **121**(3), 234–247.

Foster K R, Ziskin M C, Balzano Q & Hirata A 2020 *IEEE Access* **8**, 130239–130251.

Gibson A L F, Carney B C, Cuttle L, Andrews C J, Kowalczewski C J, Liu A, Powell H M, Stone R, Supp D M, Singer A J, Shupp J W, Stalter L & Moffatt L T 2020 *J Burn Care Res* **42**(1), 98–109.

Hasgall P A, Di Gennaro F, Baumgartner C, Neufeld E, Lloyd B, Gosselin M C, Payne D, Klingenböck A & Kuster N 2018 'IT'IS database for thermal and electromagnetic parameters

Accepted Manuscript

of biological tissues (version 4.0)'. doi:10.13099/VIP21000-04-0. Retrieved March 28, 2020, from itis.swiss/database.

Henriques F C 1947 *Arch Path* **43**, 489–502.

Hirata A, Kodera S, Sasaki K, Gomez-Tames J, Laakso I, Wood A, Watanabe S & Foster K R 2021 *Phys Med Biol* **66**(8), 08TR01.

ICNIRP 2020 *Health Phys* **118**(5), 483–524.

IEEE 2019 *IEEE Std C95.1-2019 (Revision of IEEE Std C95.1-2005 / Incorporates IEEE Std C95.1-2019 / Cor 1-2019)* pp. 1–312.

Jackson J 1999 *Classical Electrodynamics* 3rd. edn John Wiley and Sons, Inc. New York.

Knox F S, Wachtel T L & Knapp S 1979 *Burns* **5**(1), 19–29.

Kojima M, Hanazawa M, Yamashiro Y, Sasaki H, Watanabe S, Taki M, Suzuki Y, Hirata A, Kamimura Y & Sasaki K 2009 *Health Phys* **97**, 212–218.

Mattsson M O, Simkó M & Foster K R 2021 *Front Comms Net* **2**, 49.

Meyer W, Schwarz R & Neurand K 1978 *Curr Probl Dermatol* **7**, 39–52.

Miller S A, Cook M C, McQuade J S, D'Andrea J A, Chalfin S, Ziriax J, Parker J E & Beason C W 2021 *J Directed Energy* **6**(4), 299–325.

Montagna W & Yun J S 1964 *J Invest Dermatol* **42**, 11–21.

Moritz A R & Henriques F C 1947 *Am J Pathol* **23**, 695–720.

National Research Council 2011 *Guide for the Care and Use of Laboratory Animals* 8 edn National Academies Press Washington, DC.

Parker J E, Beason C W & Johnson L R 2021a *J Directed Energy* **6**(4), 408–421.

Parker J E, Beason C W, Sturgeon S P, Voorhees W B, Johnson S S, Nelson K S, Johnson L R & Whitmore J N 2020 *Health Phys* **119**, 206–215.

Parker J E, Eggers J S, Tobin P E & Miller S A 2021b *J Directed Energy* **6**(4), 388–407.

Pearce J 2009 *in* 'Proc. SPIE' Vol. 7181 of *Energy-based Treatment of Tissue and Assessment V* p. 718104.

Ponticorvo A, Burmeister D M, Yang B, Choi B, Christy R J & Durkin A J 2014 *Biomed Opt Express* **5**, 3467–3481.

Ponticorvo A, Rowland R, Baldado M, Burmeister D M, Christy R J, Bernal N P & Durkin A J 2019 *Burns* **45**(2), 450–460.

Sheldon W W 1991 Millimeter-wave exposure system augmentation Technical Report AL-TR-1991-0056 Armstrong Laboratory Brooks Air Force Base, TX.

Simonds J L, LeBegue B, Parker J E, Dayton T & Kohn N 2012 Linking predicted injury to risk of significant injury Technical Report AFRL-RH-FS-TR-2012-0024 Air Force Research Laboratory Fort Sam Houston, TX.

Stone, II R, Natesan S, Kowalczewski C J, Mangum L H, Clay N E, Clohessy R M, Carlsson A H, Tassin D H, Chan R K, Rizzo J A & Christy R J 2018 *Front Pharmacol* **9**.

Sullivan T P, Eaglstein W H, Davis S C & Mertz P 2001 *Wound Repair Regen* **9**(2), 66–76.

The HDF Group & Koziol Q 2020 'Hdf5-version 1.12.0' [Computer Software] https://doi.org/10.11578/dc.20180330.1.
URL: *https://doi.org/10.11578/dc.20180330.1*

US Department of Agriculture 2022 'USDA Animal Welfare Regulations, 9 C.F.R. Subchapter A'.
URL: *https://www.nal.usda.gov/awic/animal-welfare-act*

van Rhoon G C, Samaras T, Yarmolenko P S, Dewhirst M W, Neufeld E & Kuster N 2013 *Eur Radiol* **23**(8), 2215–2227.

Vincelette R, Shingledecker A, Roberson D, Sheldon K E, Oliver J, Washington C, Jindra N, Kornegay R W & Figueroa R 2012 A comparative study of melanin content and skin morphology for three commonly used laboratory swine (*Sus scrofa domestica*) Technical Report AFRL-RH-FS-TR-2013-0004 Air Force Research Laboratory Fort Sam Houston, TX.

Accepted Manuscript